



Microfluidic measurement of individual cell membrane water permeability

Lining Huang^a, James D. Benson^{b, **, 1}, Mahmoud Almasri^{a, *, 1}

^a University of Missouri-Columbia, MO, USA

^b Department of Biology, University of Saskatchewan, Saskatoon, SK, Canada

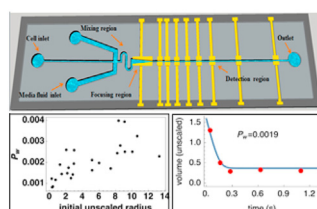


HIGHLIGHTS

- We calibrated and validated lab-on-chip dynamic cell sizing and cell membrane permeability measurements in individual cells.
- Volume-correlated impedance change of myriad individual yeast cells was rapidly measured after mixing with anisotonic media.
- Measurements were performed within 0.26 s after mixing with media from separate inlets at up to 10 electrodes over 1.3 s.

GRAPHICAL ABSTRACT

The device sequentially measures the volume-correlated impedance change of hundreds of individual yeast cells after mixing with different media, e.g. dimethyl sulfoxide or DI water, from separate inlets.



ARTICLE INFO

Article history:

Received 5 October 2020

Received in revised form

16 March 2021

Accepted 17 March 2021

Available online 12 April 2021

Keywords:

Microfluidic

Lab on a chip

Coulter counter

Yeast cell

Impedance measurement

Individual cell membrane permeability

Boyle van't Hoff

Water permeability

ABSTRACT

This paper reports a microfluidic lab-on-chip for dynamic particle sizing and real time individual cell membrane permeability measurements. To achieve this, the device measures the impedance change of individual cells or particles at up to ten time points after mixing with different media, e.g. dimethyl sulfoxide or DI water, from separate inlets. These measurements are enabled by ten gold electrode pairs spread across a 20 mm long microchannel. The device measures impedance values within 0.26 s after mixing with other media, has a detection throughput of 150 samples/second, measures impedance values at all ten electrodes at this rate, and allows tracking of individual cell volume changes caused by cell osmosis in anisotonic fluids over a 1.3 s postmixing timespan, facilitating accurate individual cell estimates of water permeability. The design and testing were performed using yeast cells (*Saccharomyces cerevisiae*). The relationship between volume and impedance in both polystyrene calibration beads as well as the volume-osmolality relationship in yeast were demonstrated. Moreover, we present the first noninvasive and non-optically-based water permeability measurements in individual cells.

© 2021 Elsevier B.V. All rights reserved.

1. Introduction

Osmoregulation and membrane mass transport is central to cell biology in bacteria, plants and animals [1–3]. It plays a role in

osmotic stress signaling in yeast [4], is critical for dialysis in the cells of the nephron [5] as well as plant water regulation [6], is a primary determinant for cryopreservation [7,8] and red blood deglycerolization success [9]. Because of this, there is a great need for accurate

* Corresponding author.

** Corresponding author.

E-mail address: almasrim@missouri.edu (M. Almasri).

¹ Corresponding authors contributed equally.

estimation of the kinetics of water and solute transport in individual cells. Mass transport models have been developed and refined since at least 1932 by Jacobs [10,11], which was followed by work by Staverman [12,13], and then formalized from a thermodynamical point of view by Kedem and Katchalsky [14,15] (among many others). In each case, however, models have depended on the challenging biophysical problem of accurate estimation of the membrane permeability parameters.

It would be beneficial for a wide range of disciplines to have the capability of rapidly estimating the water and solute membrane permeability in individual cells to identify, for example, the degree of heterogeneity in a population, or the existence of aberrant subpopulations. Moreover, there are a number of cell types that fall in the gap between microscopy methods and the classical Coulter counter method, including sperm and red blood cells, for which both mean and population distributions of membrane water and solute permeability would facilitate significant inroads in protocol design. For example, Lusianti et al. [16] show that instead of a 60-min post-thaw red blood cell deglycerolization time, detailed understanding of membrane transport kinetics and rational deglycerolization design can reduce the total time to less than a minute. However, they demonstrate that the success of this protocol critically depends on the sample (and possibly even cell) specific permeability of the RBC to glycerol [16].

Classical methods for estimation of these parameters require measurement of the dynamic total cell or cell water volume as a function of time after the exposure to anisotonic media [17], and include recording mean cell radius via light microscopy [18], fluorescence quenching in individual cells or in cell populations [19,20], or radiolabeled water diffusion via electron paramagnetic resonance [21]. Bright field microscopy methods are useful in large, individual, and slowly reacting cells, including the *Xenopus* oocytes studied by Jacobs in 1932 [22], and, now, many mammalian oocytes [23–29]. However, these microscopy methods are difficult to apply for cell populations, or for aspherical cells such as sperm or red blood cells. To avoid these complications, a number of studies use electronic particle counter (EPC) based techniques to measure these volume changes after exposure to various media [30–32].

Essential for hematology by facilitating assessment of the “complete blood count”, EPCs are ubiquitous in industrial, clinical and research settings, facilitating label free, non-optically based, rapid and accurate sizing of cells and particles [33–38]. While designed and used predominately for static particle volumes, EPCs are also used to find population level cell volume changes in response to anisotonic media. Cells in suspension are mixed in a cuvette with a different media that causes cell volume changes, and the recorded cell volume time-series facilitates population level estimation of water and solute permeability, but not for any individual cell or subpopulation [39,40]. These dynamic data can be a useful diagnostic tool for red blood cell quality assessment [41] or for the development of optimal cryopreservation protocols [42,43]. However, using commercial EPCs to make dynamic measurements requires relatively large sample volumes that limit the ability to rapidly mix and measure samples. Thus EPC technology has not been applied to dynamically size many cells including, in particular, red blood cells except in rare cases [44]. Moreover, relatively large sample volume requirements also limit the application of this technology to abundant cell types, precluding applications in rare cells, such as those obtained through cell sorting [45].

Finally, the most critical limitation of all commercially available EPC is that they are designed to make one impedance measurement on each individual cell. This is sufficient for static cells, but for those undergoing active or osmotic volume change, cell volume measurements made at any time only represent a sample from the full population at that time point. Importantly, this does not give any

insight into the distribution of biophysical responses within a cell population. It is statistically advantageous to follow many single cells' dynamics, significantly improving parameter estimation, reducing required cell counts, and importantly identifying cell membership in subpopulations. These data may be critical in hematology, as aging blood responds differently osmotically [41,46,47], and there is evidence that these subpopulations may play a role in successful rapid deglycerolization of red blood cells [44].

MEMS based EPCs [48–52] have a number of advantages over traditional benchtop devices. They are generally low cost and portable. They use small volumes of total cell suspension, and as such can provide measurements on rare cells, and should facilitate rapid measurement after mixing with anisotonic media. However, to date, no other MEMS based EPCs utilize multiple electrodes, and as such provide only traditional static cell sizing. Our device addresses these issues, and, as we show here for the first time, allows dynamic monitoring of volume changes in individual cells [53].

Biophysical modeling of cell mass transport in macroscale Coulter counters as well as in optical methods typically assumes instantaneous step-changes in extracellular media. A standard experiment may be to monitor cell volumes after cells equilibrated in isotonic media are exposed to 10% DMSO, and standard modeling assumptions are that cells experience an immediate change in their extracellular environment. This approach causes rapid and large cell volume changes that can be easily detected, facilitating accurate estimation of water and solute permeabilities. Therefore it is desirable in our device for cells to experience as instantaneous mixing as possible, especially in cell types with very high water permeability as they may partially equilibrate as the concentrations mix.

To address the need for rapid and accurate estimation of membrane water and solute permeability in individual cells, we previously developed and tested the fabrication of a multi-electrode-pair microfluidic Coulter counter with latex beads [54]. Here we refine our previous design and demonstrate our microfluidic lab on chip sensor's intended capability to measure single yeast cell water permeability and osmotic characteristics by monitoring their short time dynamic volume change after exposure to anisotonic extracellular media.

While this device has been described by us previously [55–58], this paper demonstrates the functionality of a reusable microfluidic lab on a chip for sizing dynamic particles. In particular, we describe functional testing of the operating AC frequency, demonstrate the volume-impedance relationship in both latex beads and in yeast cells, detect the real time individual cell volume change quickly after exposure to anisotonic environments, and using these volume changes, infer individual membrane mass transport biophysical characteristics. The cell volume changes are measured via voltage changes among five electrode pairs along the microchannel, yielding cell size at the time that cells pass between each electrode pair. To validate our device and demonstrate its potential, we measured microbead and yeast cell (*Saccharomyces cerevisiae*) impedance after mixing with different concentrations of anisotonic media at room temperature. To our knowledge, we are the first to report the membrane permeability of individual cells measured using a non-optical method.

2. Cell biophysical modeling

In this paper, we choose yeast cells as a test subject because of the number of existing studies of transport in common baker's yeast, with models of yeast turgor and osmotic flux (c.f [59]. for review). In particular, the differential equation describing osmotically induced total cell volume is a function of the intracellular

hydrostatic pressure p (driving water flux into the cell), and the total concentration difference across the membrane (driving water flux out of the cell):

$$\frac{dv_{os}}{dt} = L_p A \left(p - c_{pc} RT \left(c^e - c^i \frac{v_{os,0}}{v_{os}} \right) \right) \quad (1)$$

where v_{os} is osmotically active volume, L_p is water permeability, A is cell surface area, p is intracellular hydrostatic pressure that we assume to be zero, c_{pc} is a conversion factor relating pressure units to concentration units, R is the gas constant, c^e and c^i are external and internal solute concentrations, $v_{os,0}$ is the initial osmotically active volume (see Ref. [59] for derivation). Because we are using yeast cells, the application of van 't Hoff's law here includes the membrane turgor model

$$p(V, V_0, \varepsilon) = \begin{cases} -\varepsilon \ln\left(\frac{V}{V_0}\right) & \text{for } V \geq V_0 \\ 0 & \text{for } V \leq V_0 \end{cases} \quad (2)$$

where ε is a parameter and V_0 is the volume at which turgor becomes a factor [21].

This may be used in conjunction with Eq. (1) or independently to calculate v_{min} , which calculates the final minimum cell volume reached when exposed to higher concentration solute according to van 't Hoff's law, in which v_{min} is a linear function of the reciprocal of solute concentration:

$$v_{min} = v_b + \frac{c_0^i (v_i - v_b)}{c^e + c_0^e} \quad (3)$$

where v_b is the osmotically inactive volume, v_i is the initial turgid volume, c_0^e and c_0^i are the initial external and internal osmotically active solute concentrations.

In the experimental part of the paper, we collected individual yeast impedance data during volume equilibration by varying mixing media osmolality, and use these data to fit for parameters in the turgor model (Eq. (2)) and then fit the dynamic volume change Eq. (1) to calculate water permeability L_p . We compare our turgor model and fits to the literature, and L_p values to those presented in the literature.

3. Design and modeling

The microfluidic lab on a chip sensor was previously designed to detect the dynamic cell impedance changes as a function of time after mixing cell suspensions with different extracellular media as shown in Fig. 1 [55–58]. In brief, the device is capable of three major actions: fluidic mixing, cell focusing, and impedance detection. Cells introduced via a single centered inlet and extracellular media introduced via two outer inlets converge into a T-shaped channel and progress into a short serpentine shaped channel for mixing (Fig. 1). This is followed by a ramp-down electrode pair defining the focusing region. This focusing region was then connected to the measuring region, and on to the outlet. To measure volume as a function of time, we placed 10 electrode pairs along the device channel such that each electrode pair recorded the impedance of cell at the time it passed through. At constant flow rates each electrode pair corresponds to a different time point in the volume versus time dynamics of each cell or particle. Corresponding impedance changes were tracked as a function of time at each electrode pair along the channel. The distribution of electrodes along the channel was designed to take measurements more

frequently at the beginning—often the most transient phase of cell volume change.

In this paper, we have further optimized the modeling of mixing efficiency and mixing time as a function of flow rate. Our device is now capable of detecting the dynamic impedance change after mixing cell suspensions with different extracellular media within 0.26 s from the start of mixing. We also present further optimization of the fabrication processes resulting in a reliable device without any possibility of fluid leakage. Here we have calibrated our device using microbeads of six different sizes, and determined a linear relationship between bead diameter and impedance. Finally, we have demonstrated the voltage-volume relationship in *S. cerevisiae* populations and studied individual yeast cell permeability.

3.1. Microfluidic sensor Modeling

The mixing region was designed with a passive mixer (length 400 μm ; width 100 μm) facilitating diffusion-induced mixing of different extracellular media and cells. The mixer had two extracellular media channels with a width 2x larger than the cell suspension flow channel, intersecting normal to the cell suspension flow channel to significantly improve the mixing efficiency—an important factor that determines the sensitivity of system. A simulation result of mixing efficiency and mixing time versus flow rate is shown in Fig. 2. This figure indicates that at a flow rate of 0.6 $\mu\text{l}/\text{min}$, a mixing time is 0.26 s and a mixing efficiency of 97% was reached. Fig. 2 also shows that a proper flow rate must be chosen to achieve a good mixing efficiency while keep the mixing time as small as possible. The mixing efficiency and mixing time under flow rates from 0.2 to 0.9 $\mu\text{l}/\text{min}$ were simulated using the COMSOL finite element tool under a steady-state condition: a concentration of 50 mol/m^3 was set to the two outer inlets while the center inlet was set to 0 mol/m^3 . The fluid flows are set to be laminar and incompressible, and the boundary is non-slip.

3.2. Single cell detection modeling

In order to achieve both rapid measurement post mixing and an approximately 2 s transit time (time from first to last measurement) at a flow rate of 0.6 $\mu\text{l}/\text{min}$, the detection channel is designed with a length (between the first and tenth electrode) and width of 20 mm and 25 μm , respectively. It consists of gold electroplated vertical electrode pairs to generate a uniform electric field over the entire height (15 μm) of the microchannel. Each vertical electrode has a width and a length of 100 μm and 100 μm , respectively. In device testing, cells suspended in media flow between a pair of electrodes.

The detection region in our device has 10 electrode pairs measuring the voltage across the channel and the associated voltage change when a particle passes through, ΔV , can be converted to impedance change (ΔZ) as a function of time. The relation between voltage and impedance change is given by

$$\frac{\Delta Z}{Z_{ch}} = \frac{\Delta V}{V_{ch} G_{amp}} \quad (4)$$

where ΔZ is the impedance change when a particle passes between the electrode pair, Z_{ch} is the baseline impedance between the electrode pair without a particle V_{ch} is the baseline voltage between an electrode pair of the channel without a single particle passing through, and G_{amp} is the amplifier gain in the testing circuit.

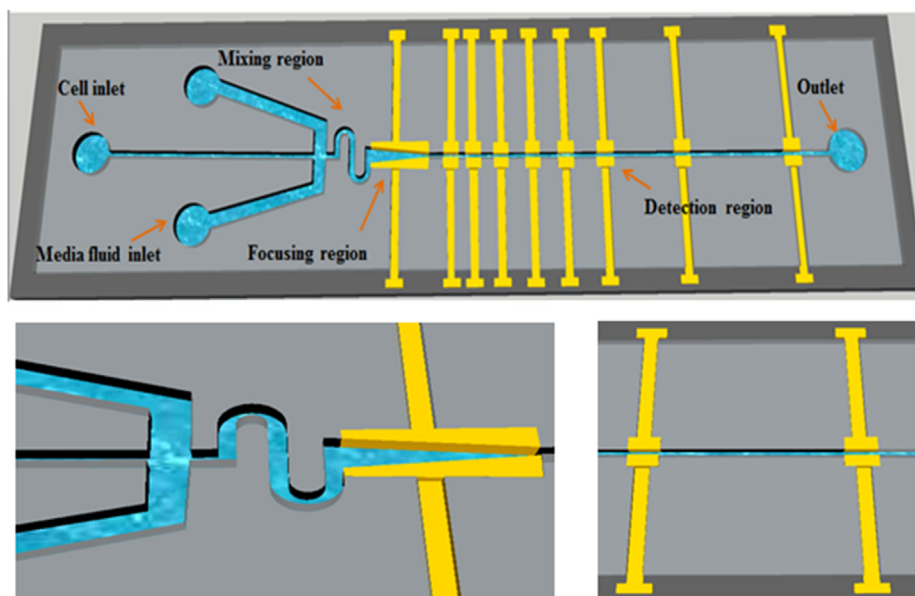


Fig. 1. Microfluidic Lab on a chip sensor structure: (a) Schematics of the microfluidic Lab on a chip sensor structure. The blue color microchannel has three inlets intersecting into a T-shape micromixer, and yellow color electrode pairs are positioned along the channel. (b) A magnified view of the mixing region, focusing region and detection region. A ramp shaped electrode pair generates a negative dielectrophoresis (n-DEP) forces that are used for focusing mechanism, gold electroplated vertical electrodes with a height of 15 μm are used for detecting particles passing through. (For interpretation of the references to color in this figure legend, the reader is referred to the Web version of this article.)

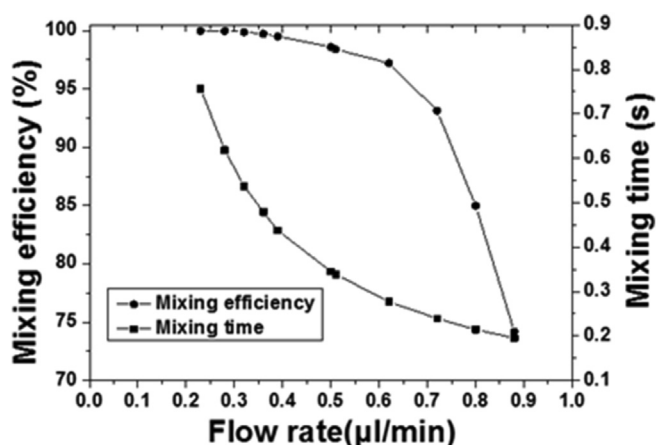


Fig. 2. The results from a COMSOL simulation of the mixing efficiency and mixing time as a function of flow rate. At a flow rate of 0.6 $\mu\text{L}/\text{min}$, a mixing time is 0.26 s and a mixing efficiency of 97% was reached. The mixing efficiency is a tradeoff with mixing time.

4. Microfluidic lab a chip device fabrication

As described previously [60], the device fabrication process includes thin film sputtering, metal electroplating, SU-8 channel lithography and patterning, and PDMS bonding. The devices were fabricated with a height different from our previous devices, and the fabrication process was optimized to develop more reliable devices. Fabrication started with a single glass slide as follow. (1) A thin layer of SU-8 was spin coated with a thickness of 3 μm , exposed to UV light for 10 s, and hard baked for 30 min. This was followed by UV light exposure to form an adhesion layer for future SU-8 microchannel bonding. This layer was used in order to improve the adhesion between the glass substrate and the subsequent SU-8 layer that is used to form the microchannel. (2) Two layers of chromium (Cr) and gold (Au) were deposited using

magnetron sputtering (See Fig. 3a). The Au layer was patterned, using Shipley 1813, and potassium iodine Au Etchant solution of $\text{K}:\text{I}_2\text{H}_2\text{O} = 4:1:40$, to form a seed layer for electroplating, electrode traces and bonding pads. The thickness of Cr and Au were 60 nm and 200 nm, respectively. (3) A photoresist mold was formed using AZ4620 photoresist (See Fig. 3a') and Au with a thickness of 15 μm was electroplated to create the focusing and detection electrode pairs. (4) The AZ photoresist was washed away by acetone followed by IPA and DI water, and the Cr layer was etched (See Fig. 3b and b'). (5) The microchannel was defined using SU-8 2025 with a thickness of 20 μm . Before SU-8 photoresist coating, the slides were flashed with IPA thoroughly and dried. After patterning, the microchannel was hard baked on a hotplate at 150 $^\circ\text{C}$ for 30 min to further stabilize the feature and completely remove the remaining solvent (Fig. 3c and c'). Scanning Electron micrographs (SEMs) of the device are shown in Fig. 4. (6) PDMS slabs were made to serve as a top cover for the device along with fluidic connectors. The PDMS was initially mixed with its curing agent and poured into petri-dish with/without fluidic connectors glued vertically to them at the locations corresponding to the inlet and outlets, and was cured overnight. The PDMS slab without fluidic connectors was punched through to form an opening for the inlets and outlet. (7) An oxygen plasma treatment was applied on the PDMS cover (without fluidic connectors) to create silanol groups (-OH) in order to change its surface to hydrophilic and then SU-8 was spin coated onto it to serve as glue. This SU-8 layer was used in order to make an adhesion layer between microchannel and bottom PDMS slab. (8) The microchannel was then aligned with the PDMS cover manually. A pressure was applied to the PDMS slab to form strong bond with bottom SU-8 channel. Then, the device was exposed to UV light for 30 s and hard baked at 120 $^\circ\text{C}$ for 20 min to improve the bonding by further curing the SU-8 layers. Thus, the PDMS/SU-8 cover was cross-linked with the SU-8 microchannel, forming a strong bond (Fig. 3d). Then after connectors (barbed connectors 1/16" to 1/16" black nylon) and tubes (1/16" ID x 1/8" OD x 1/32" wall silicone Med-X tubing, United States Plastic Corporation) were bonded into top PDMS slab, both of the top PDMS and the device were treated

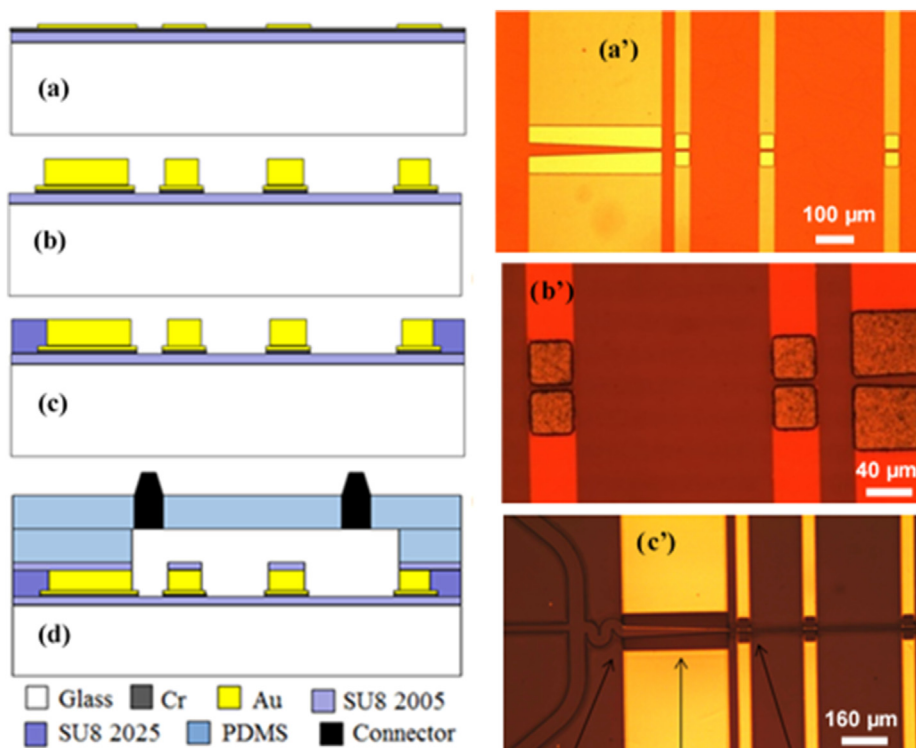


Fig. 3. Microfluidic lab on a chip device fabrication process and its corresponding optical images: (a) Cr and Au patterning for electrode layer (b) Au electroplating and Cr etch (c) SU-8 microchannel patterning (d) PDMS and fluid connector cover (a') corresponding optical images for fabrication step a (b') corresponding optical images for fabrication step b (c') corresponding optical images for fabrication step c.

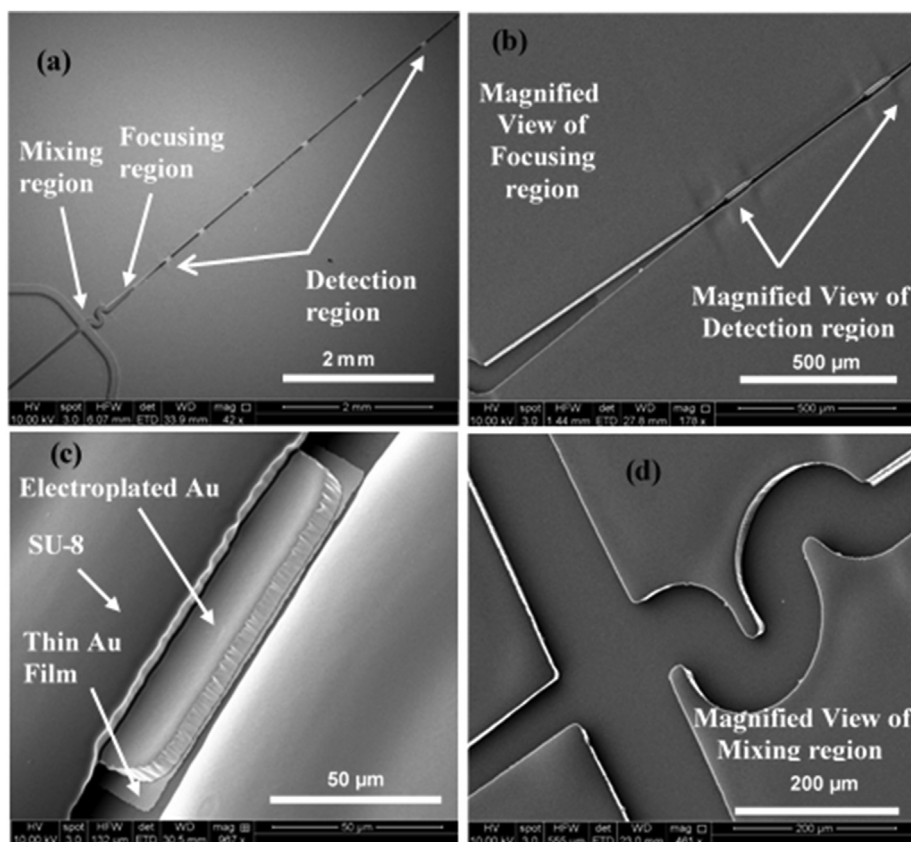


Fig. 4. SEM micrographs of (a) the fabricated microfluidic sensor before sealing the device with PDMS cover, (b) a magnified view of focusing and detection regions, (c) a single detecting electrode, (d) a magnified view of mixing region.

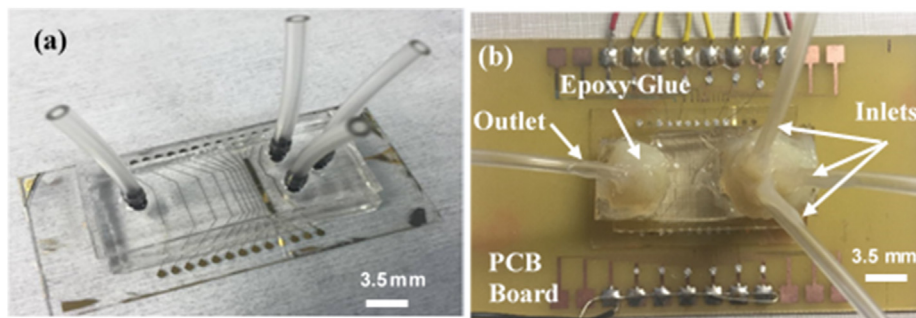


Fig. 5. Optical images of the fabricated microfluidic sensor. (a) A finished device, and (b) a packaged device.

with oxygen plasma, creating silanol groups to yield a covalent bond between two PDMS slabs and seal them tightly (Fig. 5a). (10) The device was fixed and wire bonded to PCB for electrical connections. Finally, the SU-8 biocompatible treatment was performed by using a 30 s flood of UV exposure at 14.75 mW/cm^2 , followed by hotplate baking at $150 \text{ }^\circ\text{C}$ degree for 1 h, and then an oxygen plasma treatment for 30 s. Epoxy glue was used to improve the reliability of the device, and to eliminate any leakage possibility between connectors and PDMS cover (Fig. 5b).

5. Validation and testing

5.1. Experimental setup

The experimental testing setup consists of the following (See Fig. 6a). Two syringe pumps (Harvard Apparatus PHD ULTRA, Harvard Apparatus) with two syringes (3 mL Syringe Sterile with Luer

Slip Tip, BH Supplies) were used to inject the cells or microbeads from the center inlet and extracellular media into the outer two inlets. Two function generators (Hewlett Packard 33120A) were used to apply an AC signal for both the focusing and detection electrodes. One DC power supply (Agilent E3646A) was used to supply DC voltage to the instrumentation amplifier (Analog Devices AMP02). An inverted microscope was used to observe the mixing region, focusing region, cells flowing in the microchannel, and the electrode pair condition. In addition, we have designed and built an electrical circuit to measure the impedance changes of microbeads and cells in the detection region (Fig. 6b). An AC signal was applied to the device that was connected to a voltage divider. The real time voltage data across the channel was amplified by an instrumentation amplifier, filtered using a high pass filter and recorded using a data acquisition board (NI, DAQ USB-6216). Using National Instruments Labview and an AC voltage source, we tracked the impedance of latex beads and individual yeast cells as they flowed through the channel between five (of the ten) electrode pairs (pairs 1, 2, 3, 6, and 10). Prior to impedance measurements using the detection electrode pairs, an AC source with 6 V peak to peak at 10 MHz was applied to the focusing electrode pair in order to generate a p-DEP force to focus the microbeads or cells to the centerline of the channel.

5.2. Cell Culture and experimental solutions

Commonly available Fleischmann's ActiveDry Yeast was used as the experimental cell type. For cell culture, the dry yeast were placed in warm water ($55 \text{ }^\circ\text{C}$) with 5% sucrose overnight at room temperature. After overnight cultivation and growth, yeast cell aggregates and debris drop down to the bottom of the container leaving a single cell suspension in the clearer fluid at the top. The yeast cell stock solution was extracted from clearer fluid from top of the cultivation container. Prepared 10x PBS (phosphate buffered saline; Sigma-Aldrich) was diluted with DI water into the required final PBS concentrations. The experimental yeast cell suspensions were formed with 3 mL yeast cell stock solution and 20 mL of the PBS solution. The microbeads and yeast cell concentrations varied from around 10^6 to 10^8 cells/mL, and most experiments were conducted at around 10^7 cells/mL.

5.3. Frequency analysis

Latex microbeads (Beckman Coulter) with a diameter of $5 \mu\text{m}$ in DI water were injected into inlets, and the voltage change under four different operating frequencies 100 Hz, 1000 Hz, 10 kHz and 100 kHz were measured to determine optimal AC source frequency for cell volume impedance measurement.

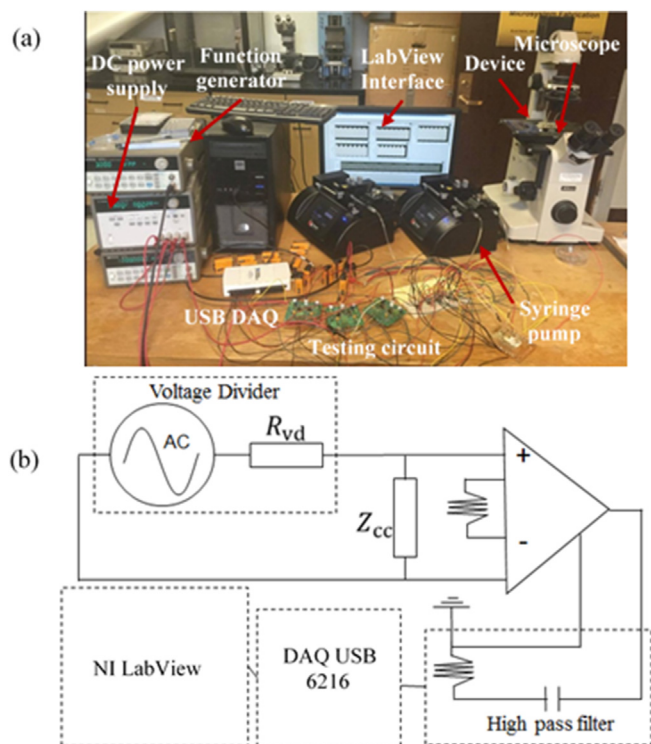


Fig. 6. (a) The experimental testing setup. The arrows and captions indicate each component. (b) The electrical testing circuit for one channel. In particular, the device is connected to a voltage divider, resulting impedance data is filtered by a high pass filter and then is recorded by USB DAQ.

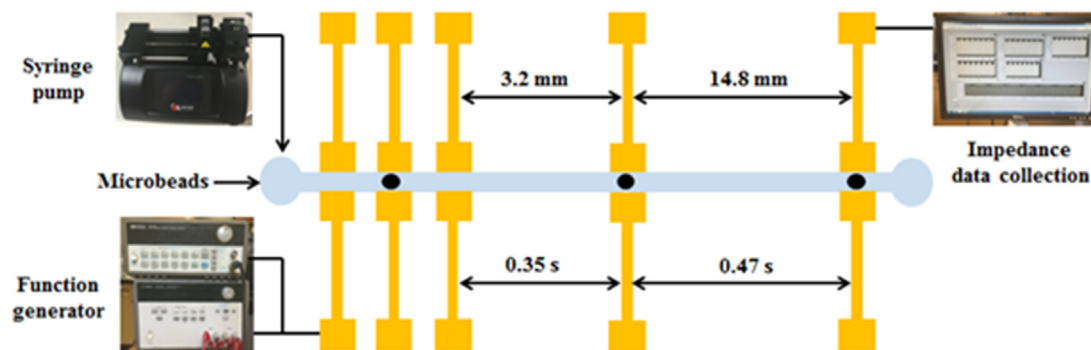


Fig. 7. Schematic illustration of impedance as a function of time over five channels: beads going through all five electrode pairs as a function of time with a flow rate of $0.4 \mu\text{l}/\text{min}$.

5.4. Establish impedance-volume relationship and electrode-to-electrode variability

Latex microbeads with diameters of $4 \mu\text{m}$, $6 \mu\text{m}$, $8 \mu\text{m}$, and $10 \mu\text{m}$ (Sigma-Aldrich) and $5 \mu\text{m}$ (Beckman Coulter) in $1\times$ PBS were measured with the device set up to use a series of five (of the ten) electrode pairs (see Fig. 7). The inter-electrode-pair transit time was calibrated by using the initial voltage peak at each electrode-pair along the channel. Subsequent signals for individual beads were correlated among the five electrode pairs by this transit time estimate. Variation in transit time among channels was estimated.

5.5. Volume testing in yeast cells

Isolated yeast cells suspended in $1\times$ PBS were injected into the center channel while the two outer media ports were injected with $0.75\times$, $1\times$, $1.5\times$, $2\times$, $3\times$, $5\times$, $6\times$ and $10\times$ PBS. Because each outer inlet media flow volumes is 10 times bigger than the volume flow of the cell inlet, the resulting post-mixing concentration will be equivalent to the outer media concentration, a result confirmed by COMSOL Multiphysics 3.5a simulation. Five electrode pairs were used to record the voltage change as cells passed through the electrodes for each concentration. Cell volumes were estimated using the impedance-volume relationship defined in the previous experiment, initial isosmotic cell volumes were assumed to be given by the value at the first electrode pair (approximately 0.26 s after onset of mixing with the anisosmotic media), and the equilibrium volume was defined to be the average of the final two electrode pair values. To validate these results, yeast in $1\times$, $1.5\times$, $3\times$, $5\times$, and $10\times$ PBS were placed on glass slides with coverslip and imaged at $40\times$ magnification. Resulting photomicrographs (see Fig. S1) were analyzed for particle volume assuming elliptical shape in Ref. [60], where all visible particles, regardless of size and shape were identified and volume was calculated by finding the equivalent spherical radius from the measured area.

5.6. Measurement of water permeability in yeast cells

Yeast cells in $1\times$ PBS were injected into the center channel, and 10% dimethyl sulfoxide (DMSO; Sigma-Aldrich) dissolved in $1\times$ PBS was injected into the outer two channels. We have used five electrode pairs (pairs 1, 2, 3, 6, and 10) to track the yeast cell volume change as a function of time with maximum measuring frequency. The resulting volume versus time data for individual yeast cells at 23°C were fit using the water transport model defined in Eqs. (1) and (2). Note that in our hands the yeast cells have an inherently large variation in volume and thus SA:V ratio, which directly affect the water permeability term P_w . We used DMSO as our osmolyte to

maintain constant electrolyte concentrations for experiments. DMSO is membrane permeable to most cells, but we neglect its contribution to the intracellular osmolality because during the approximately 2 s post mixing measurement the DMSO permeation into the cell that would affect the intracellular total osmolality is minimal, and thus the estimation of P_w is unaffected. This is in line with protocols used by, for example Schaber and Klipp who use membrane permeable glycerol as the relatively impermeant osmolyte [58]. Yeast have an extremely high hydraulic conductivity (Dumont et al., 2004) [61], and as such, their osmotic response in the short term will be dominated by the loss of water, as evidenced in our study. This is exacerbated by the large surface area to volume ratio of the relatively small yeast cells.

6. Results

6.1. Frequency analysis

Voltage amplitude as a function of frequency is shown in Fig. 8. In particular, we found that the voltage change amplitude at 100 Hz frequency is large but with a standard deviation (STD) of almost 0.6 Hz corresponding to relatively inaccurate volume estimation. For higher frequencies above 10 KHz , the standard error is very small but the voltage change amplitude is also small, reducing the device sensitivity. Furthermore, from eqn. (3) in the modeling part,

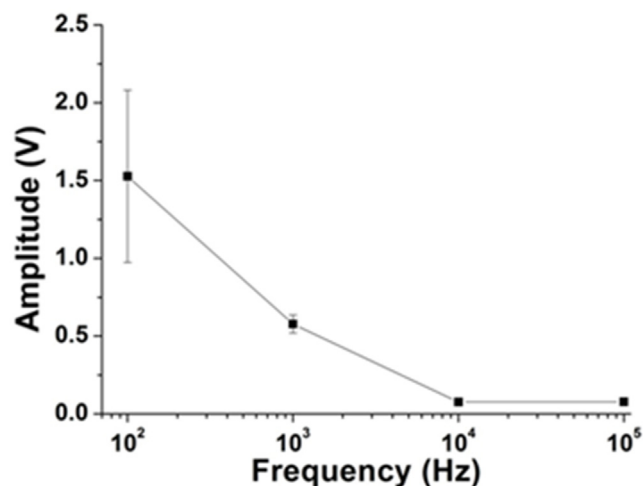


Fig. 8. Mean voltage amplitude and STD for $5 \mu\text{m}$ diameter latex beads under different operating frequencies. While the mean amplitude is bigger at lower operating frequency, its SEM is proportionately large. On the other hand, the mean amplitude is smaller while SEM is also smaller under higher operating frequency.

when particle diameter is comparable to microchannel width, stray capacity, double layer resistance and cell impedance dominate overall particle resistance between electrode pairs. Though we use DI water as the carrier media in this experiment, the result should be applicable to other carrier media. Therefore, we have selected the 1 kHz operating frequency, balancing sensitivity and precision.

6.2. Establish impedance-volume relationship and electrode-to-electrode variability

Example voltage responses to latex microbeads at all five electrodes are shown in Fig. 9. The mean \pm SEM of measured voltage of the five microbead sizes, at each electrode pair, are shown in Fig. 9a and Table 1. After multiple regression, we found that mean

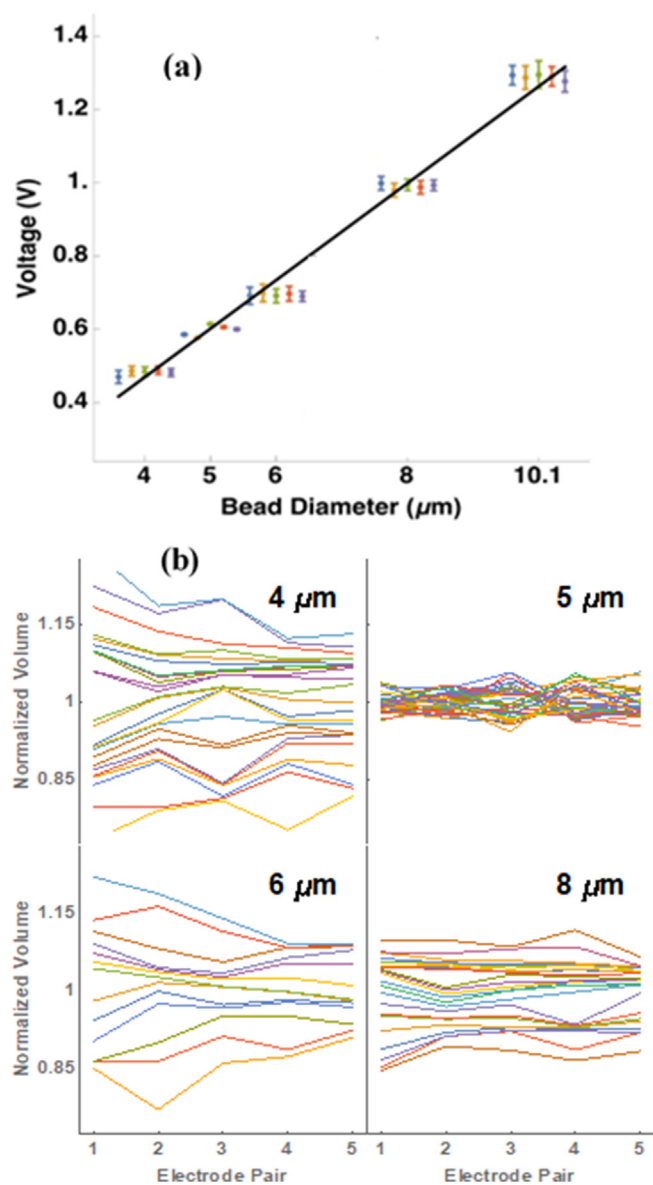


Fig. 9. (a) Mean \pm SEM value of voltage as a function of bead diameter and electrode pair (note that groups of five points at each bead diameter all correspond to the same diameter). At each bead diameter, individual beads were measured at five electrode pairs, corresponding to five distributions. b) Normalized traces of individual bead volumes through five electrode pairs. There is inherent variance in bead diameter but the small electrode-to-electrode variance is shown by the nearly parallel traces along the channel.

Table 1

Mean voltage value and sem data for different sizes of microbeads in five electrode pairs of experiment b.

Size (μm)	Mean (V)	SEM
4	0.47	0.007
5	0.60	0.009
6	0.69	0.010
8	0.99	0.009
10.1	1.24	0.013

impedance increased linearly with diameter and there was no mean difference among electrode pairs ($R^2=0.92$, $p < 0.05$ for all data). Moreover, in Fig. 9b, we show repeated measurement of 4 μm and 8 μm beads through all five electrode pairs normalized to the initial impedance of the first electrode pair. The percent error of the volume normalized mean among electrodes for all bead sizes was 1%, and mean \pm SE for each bead size along all electrodes is given in Table 1. Note that the 5 μm beads are from a different distributor with tighter bead-size tolerance (Beckman Coulter, Inc.), attesting to the fact that the measurement errors are attributable to intrinsic bead size differences and not our device.

6.3. Volume responses of yeast cells

The yeast cell volumes were compiled in a Boyle van 't Hoff plot (Fig. 11), where normalized equilibrium cell volumes are plotted against the inverse relative PBS concentration. We fit our data to a turgor model presented in Ref. [59] using eqn. (2), finding the volume concentration relationship and found a non-turgid volume, V_0 , of 72% and a non-osmotically active volume, V_b , of 42%, and a ratio of initial turgor to the elastic modulus, P_0/ϵ , of 1.12. The impedance curves in Fig. 10 and Fig. 11 demonstrate expected smooth impedance changes indicating that the cells were stressed or not damaged. To wit, a cell that is not membrane-intact will not respond osmotically. This provides both a quality assurance and a diagnostic tool. We did not recover cells after measurement to check for cell viability.

6.4. Measurement of water permeability in yeast cells

Sample yeast volume responses to DMSO data and best fits to the model defined in equation (6) are shown in Fig. 10a and the results for individual yeast cells as a function of fit initial radius are shown in Fig. 10b. The results show the impedance of yeast cells decreases for the first 3 electrodes, corresponding to the first 0.3 s after initial volume change before the cells reached quasi-equilibrium. Fig. 10 demonstrates that the time intervals between the measured impedance from different electrodes are proportional to the distance between them. This result clearly indicates stable and successful control of flow rate.

7. Discussion

In our experiments, impedance data is collected when single particle passes through an electrode pair at a time point as illustrated in Fig. 7. Because of the different spacing between electrode pairs, the impedance data are also collected at different time points accordingly.

In the frequency analysis experiment, microbeads are used instead of cells because of their uniform sizes that can be used to calibrate the device. We have tested yeast cells at 1 kHz in all relevant carrier fluids. From the following experiment B, C, D data, there is no obvious amplitude value or error bar shift, so these data suggest that this AC frequency can also be applied to different kinds

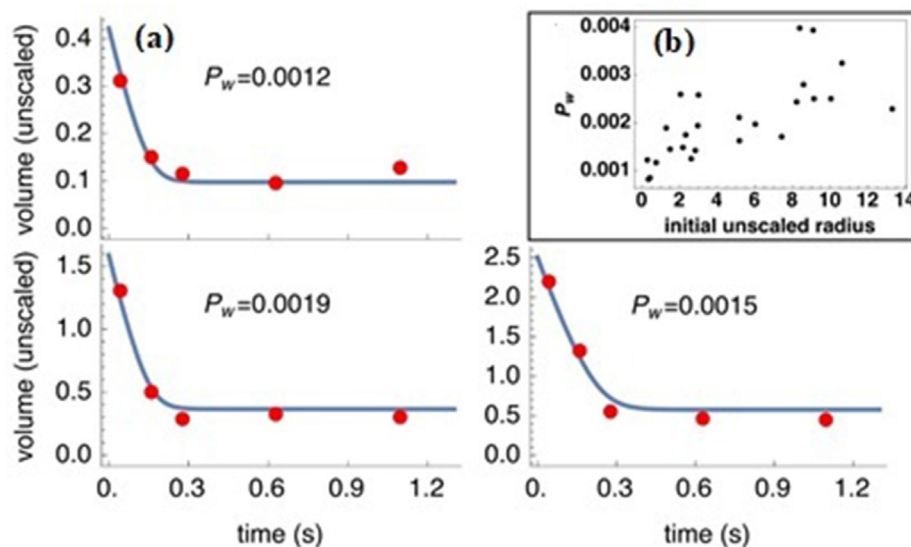


Fig. 10. (a) Representative plots of individual yeast cell volumes (dots) as a function of time after exposure to 10% DMSO. Each time point corresponds to a yeast cell passing one of the five electrode pairs. Best fit curves are shown and the unscaled permeability value is given. (b) The aggregated best fit unscaled water permeability is given as a function of initial unscaled radius.

and concentration of solutes. In our volume calibration experiment, we found the mean voltage change value increases linearly with bead diameter [62]. This is not the same as would be expected of conventional Coulter counter designs [59], but has been observed in other microfluidic EPC.

The almost parallel lines shown in Fig. 9b and the small percent error of the mean (~1%) demonstrate that the five electrode pairs have the ability to measure voltage change, and thus particle or cell volume, consistently. Finally, the ability to resolve differences in intrinsic population variance demonstrated by the difference between the standard error in the beads sourced from two different sources, we believe that much of the voltage change error can be attributed to the intrinsic bead size population differences from different distributors.

While a number of reports of MEMS devices to count cells exist, to our knowledge, the specific volume relationship sought in this manuscript for MEMS coulter counters has only been studied with beads [62], where Richards et al. report that voltage change is proportional to diameter. This is counter to the usual expectation from the Coulter principle that voltage change is proportional to particle volume. However, this difference is explained in part by DeBlois et al. (1977) [63] who define the voltage response as an unknown function of bead diameter to channel width that amounts to a fairly linear response when bead diameter is close to aperture diameter [63].

To validate our intended application, dynamic sizing of living cells undergoing rapid volume changes, we used commonly available yeast cells. There have been a number of studies investigating the osmotic properties of yeast, and coupled with their ease of procurement, they seemed to be an ideal test case. We fit the response of yeast cells equilibrated in anisotonic saline (PBS) solutions to Eqs. (1) and (2) to determine the relationship between volume and concentration in a Boyle van 't Hoff plot shown in Fig. 11. Yeast are nonlinear osmometers, and as such evince a turgor upon swelling past a critical volume. We found that when all particles were included in the analysis, there was a very large range of values of particles that were osmotically active (and thus were assumed cells) that upon careful inspection of the photomicrographs, seem to be liposomes, micells, etc. That our device detects debris is not surprising, and we are not the first to measure the

osmotic response of such debris with a Coulter counter. In fact, Higgins and Karlsson (2008) [64] found similar effects of osmotically active debris using a benchtop Coulter counter and mouse insulinoma cells. The unfiltered data, when fit to the turgor model provided by Schaber and Klipp [58], suggest a too-low osmotically inactive volume. However, when a threshold protocol similar to that proposed by Higgins and Karlsson [64] was applied, mean volumes (as measured by microscopy) and, importantly the osmotic response align fairly well literature values (see Fig. 11B). In Fig. 11B, we note that there is some difference in 1.5x and 3x PBS anisotonic media. This discrepancy at these tonicities could be due to the changing impedance of the carrier media, or it could be due to the inherent challenges in estimating volumes from photomicrographs when the cells are not spherical. It is promising, however, that the minimal volume when regressed to infinite osmolality is equal to that given by both literature and our own photomicrograph data.

In the present manuscript, this leads to a complicated interpretation. On one hand, our bead data have an undeniably linear voltage-diameter relationship aligning with Richards et al. (2012) [62], but using this to determine calibration factors for yeast data lead to predicted yeast volumes that are orders-of-magnitude too large for yeast (c.f. Bryan et al., 2010) [65], and volume changes that were too great upon exposures to anisotonic conditions [58]. However, because our MEMS voltage data, when treated as proportional to volume for unfiltered yeast cells, aligned remarkably with volumes obtained via photomicrographs, and that when these data were high-pass filtered at a minimal volume threshold they align nearly perfectly with the published relative volume response of yeast [58], we conclude that our device is working as intended to identify the volume response of individual cells. We don't have a theoretical explanation for why this could be different in cells, but it could be due to double layer resistance, stray capacitance effects, effects of organelles, etc. whose effects on predicting volume responses in cells are not explored in the MEMS literature and are not relevant in the larger scale benchtop Coulter counter literature.

Our cell suspensions are quite dilute, and as such, clumping is not likely. Moreover, after conducting a number of trials where cells were passed through the channel while observing through a microscope, we have not observed any cell clumping during

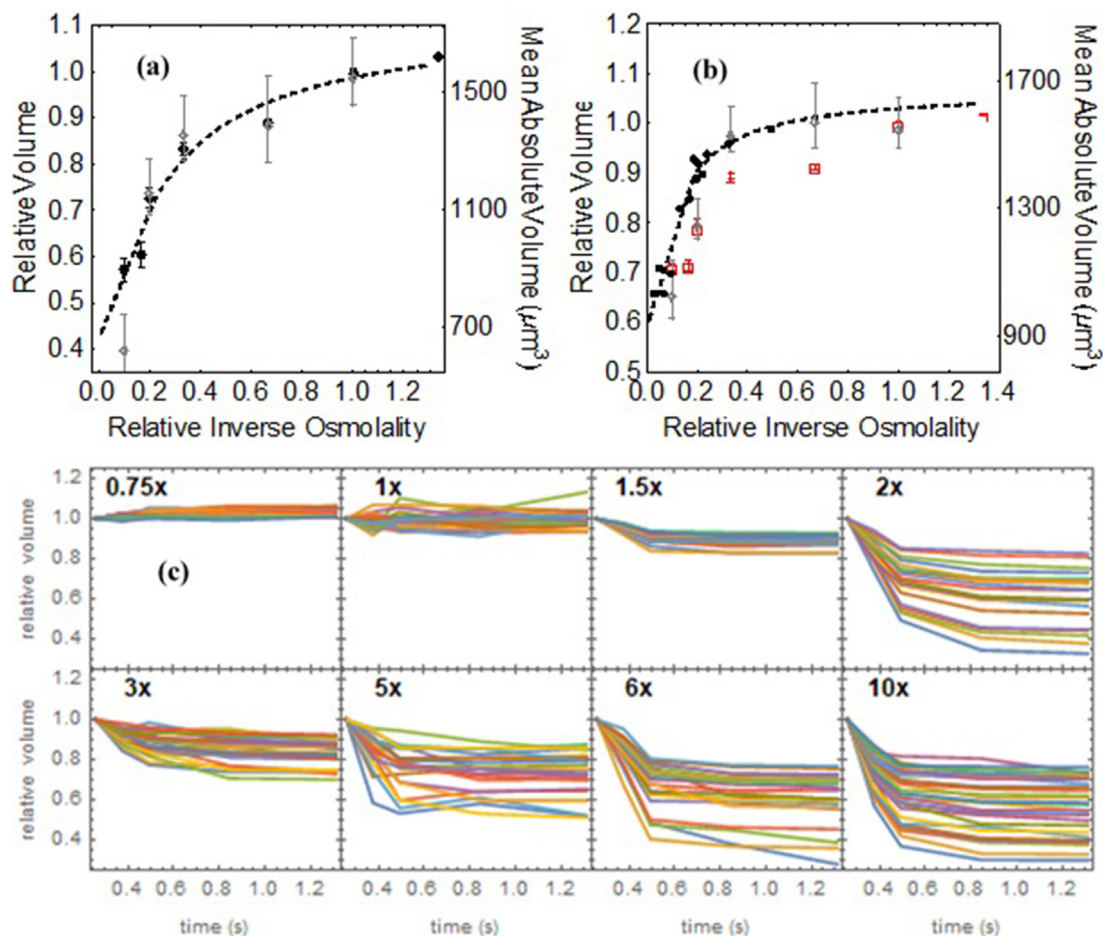


Fig. 11. A) Boyle Van 't Hoff plot of yeast measured in the MEMS Coulter counter (black markers) and corresponding photomicrograph obtained values (grey markers). Mean equilibrium relative cell volume ($V_{\text{final}}/V_{\text{initial}}$, where individual volume traces are shown in (C)) is plotted as a function of inverse relative PBS concentration, error bars indicate SEM. A nonlinear regression with Eqs. (2) and (3) was performed with free variables V_0 , V_b , V_i , and ϵ , where these parameters are defined elsewhere. Here we found $V_0 = 0.72$, $V_b = 0.42$, $V_i = 1.79$, and $\epsilon = 11,180$. B) Same as A, except with a high-pass volume filter applied, and volume data from Schaber and Klipp [58] (solid circles), a regression was applied and here we found $V_0 = 0.90$, $V_b = 0.59$, $V_i = 2.12$, and $\epsilon = 47,300$. A high pass filter was applied to the MEMS data, shown with red squares, where error bars indicate SEM. C) The individual volume traces that give volume responses to listed "xPBS" concentrations. Each color indicates an individual cell response over time. (For interpretation of the references to color in this figure legend, the reader is referred to the Web version of this article.)

measurement and data analysis. The device is washed for 1 h to clear any cells or solution from the channel, and then reused. In this project, the device was reused many times over a period of two weeks to measure the voltage of microbeads with various diameters. There is no lower limit to cell concentration, and the upper limit will be only limited by the relationship between spacing, flow rate, and data handling capabilities. Throughput, in theory, has no limitation, as higher fluid flow rates can be achieved by extending the length of the channel proportionately, allowing higher flow rates with the same transit time. However the flow rate is bounded by the concomitant pressure increase that will eventually result in cell death.

The impedance curves in Fig. 10a demonstrate expected smooth impedance/cell volume changes indicating that the cells were not damaged. This provides both a quality assurance and a diagnostic tool. Moreover, if cells are damaged during measurements, the device design can be modified by changing the driving pressure, and channel dimensions until such damage is eliminated. The figure also demonstrates that the time intervals between the measured impedance from different electrodes are proportional to the distance between them. This result clearly indicates stable and successful control of flow rate. We believe that these are the first reports of individual cell permeabilities using electrical impedance

techniques and we anticipate that any mammalian cell type will be considerably more uniform in volume than yeast, as it has been shown that yeast do not behave as linear osmometers throughout the osmotic range, confounding analysis compared to what is expected for RBC.

8. Conclusion

A microfluidic sensor has been designed, fabricated and tested, five electrodes' voltage change data were recorded and plotted for 6 sizes of microbeads to calibrate the device and validate there is no mean voltage change difference between each electrode pair. The calibration testing result shows that voltage change amplitude has a linear relationship between particle diameters. Yeast cells suspended in 1x PBS mixed with 10% DMSO and different concentration PBS solutions were monitored with five electrode pairs to study single cell permeability and biophysical characteristics. The results for individual yeast cells as a function of a fit initial radius was also demonstrated. The results show that this device has the capability to differentiate particles based on their sizes and monitor real time single cell volume change within 0.26 s from initial mixing for single cell permeability and biophysical characteristic study.

CRediT authorship contribution statement

Lining Huang: contributed to, Investigation, Data curation, Formal analysis, Methodology, Writing – original draft, Writing – review & editing. **James D. Benson:** contributed to, Conceptualization, Data curation, Formal analysis, Investigation, Methodology, Project administration, Writing – original draft, and, Writing – review & editing. **Mahmoud Almasri:** contributed to, Conceptualization, Funding acquisition, Methodology, Project administration, Resources, Supervision, Writing – original draft, and, Writing – review & editing.

Declaration of competing interest

This work has not been published previously, and it is not under consideration for publication elsewhere. The publication is approved by all authors, and if accepted, it will not be published elsewhere in the same form, in English or in any other language, including electronically without the written consent of the copyright-holder.

Acknowledgements

Funding for this research was provided in part by the University of Missouri internal funding, the National Science and Engineering Research Council (RGPIN-2017-06346 to JB), and the Saskatchewan Health Research Foundation (to JB). The second and third authors have equal contribution.

Appendix A. Supplementary data

Supplementary data to this article can be found online at <https://doi.org/10.1016/j.aca.2021.338441>.

References

- [1] P.H. Yancey, M.E. Clark, S.C. Hand, R.D. Bowlus, Living with water stress: evolution of osmolyte systems PH Yancey, *Science* 217 (1982) 1214–1222.
- [2] W. Stein, W. Lieb, Transport and Diffusion across Cell Membranes, *Academic Press Inc*, 1985, ISBN 0-12-664660-0.
- [3] A. Finkelstein, Water Movement through Lipid Bilayers, Pores and Plasma Membranes: Theory and Reality, *Wiley-Interscience*, 1987, -10: 0471847879.
- [4] E. Klipp, B. Nordlander, R. Krüger, P. Gennemark, S. Hohmann, Integrative model of the response of yeast to osmotic shock, *Nat. Biotechnol.* 23 (2005) 975–982.
- [5] S. Nielsen, B.L. Smith, E.I. Christensen, M.A. Knepper, P. Agre, CHIP28 water channels are localized in constitutively water-permeable segments of the nephron, *J. Cell Biol.* 120 (1993) 371–383.
- [6] M. Christophe, Aquaporins and water permeability of plant membranes, *Annu. Rev. Plant Physiol. Plant Mol. Biol.* 48 (1997) 399–429.
- [7] P. Mazur, Freezing of living cells: mechanisms and implications, *AJP - Cell Physiology* 247 (1984) 125–142.
- [8] P. Mazur, Equilibrium, quasi-equilibrium, and nonequilibrium freezing of mammalian embryos, *Cell Biophys.* 17 (1990) 53–92.
- [9] R.E. Lusianti, J.D. Benson, J.P. Acker, A.Z. Higgins, Rapid," removal of glycerol from frozen-thawed red blood cells, *Biotechnol. Prog.* 69 (2013) 609–620.
- [10] M. Jacobs, The simultaneous measurement of cell permeability to water and to dissolved substances, *J. Cell. Comp. Physiol.* 2 (1932) 427–444.
- [11] M.H. Jacobs, D.R. Stewart, A simple method for the quantitative measurement of cell permeability, *J. Cell. Comp. Physiol.* 1 (1932) 71–82.
- [12] A. Staverman, The theory of measurement of osmotic pressure, *Recueil des travaux chimiques des Pays-Bas* 70 (1951) 344–352.
- [13] A. Staverman, Non-equilibrium thermodynamics of membrane processes, *Trans. Faraday Soc.* 48 (1952) 176–184.
- [14] K. Ora, A. Katchalsky, Thermodynamic analysis of the permeability of biological membranes to non-electrolytes, *Biochim. Biophys. Acta* 27 (1958) 229–246.
- [15] O. Kedem, A. Katchalsky, A physical interpretation of the phenomenological coefficients of membrane permeability, *J. Gen. Physiol.* 45 (1961) 143–179.
- [16] A. Verkman, A. VanHoek, T. Ma, A. Frigeri, W. Skach, A. Mitra, B. Tamarappoo, J. Farinas, Water transport across mammalian cell membranes, *Am. J. Physiol. Cell Physiol.* 270 (1996) C12–C30.
- [17] H.-H. Chen, H. Shen, S. Heimfeld, K.K. Tran, J. Reems, A. Folch, D. Gao, A microfluidic study of mouse dendritic cell membrane transport properties of water and cryoprotectants, *Int. J. Heat Mass Tran.* 51 (2008) 5687–5694.
- [18] A.F. Davidson, C. Glasscock, D.R. McClanahan, J.D. Benson, A.Z. Higgins, Toxicity minimized cryoprotectant addition and removal procedures for adherent endothelial cells, *PLoS One* 10 (2015), 0142828, 0142850.
- [19] A.K. Fry, A.Z. Higgins, Measurement of cryoprotectant permeability in adherent endothelial cells and applications to cryopreservation, *CM* 5 (2012) 287–298.
- [20] S.I. Pascu, P.A. Waghorn, B.W.C. Kennedy, R.L. Arrowsmith, S.R. Bayly, J.R. Dilworth, M. Christlieb, R.M. Tyrrell, J. Zhong, R.M. Kowalczyk, D. Collison, P.K. Aley, G.C. Churchill, F.I. Aigbirhio, Fluorescent copper(II) bis(thiosemicarbazones): synthesis, structures, electron paramagnetic resonance, radiolabeling,, in: *Vitro Cytotoxicity and Confocal Fluorescence Microscopy Studies* vol. 5, ACES, 2010, pp. 506–519.
- [21] M. Jacobs, The simultaneous measurement of cell permeability to water and to dissolved substances, *J. Cell. Comp. Physiol.* 2 (1932) 427–444.
- [22] Y. Agca, J. Liu, A. Peter, E. Critser, J. Critser, Effect of developmental stage on bovine oocyte plasma membrane water and cryoprotectant permeability characteristics, *Mol. Reprod. Dev.* 49 (1998) 408–415.
- [23] C.T. Benson, J.K. Critser, Variation of water permeability (Lp) and its activation energy (Ea) among unfertilized golden hamster and ICR murine oocytes, *Cryobiology* 31 (1994) 215–223.
- [24] D. Gardner, C. Sheehan, L. Rienzi, M. Katz-Jaffe, M. Larman, Analysis of oocyte physiology to improve cryopreservation procedures, *Theriogenology* 67 (2007) 64–72.
- [25] J.O. Karlsson, A.I. Younis, A.W. Chan, K.G. Gould, A. Eroglu, Permeability of the rhesus monkey oocyte membrane to water and common cryoprotectants, *Mol. Reprod. Dev.* 76 (2009) 321–333.
- [26] S.F. Mullen, M. Li, Y. Li, Z.-J. Chen, J.K. Critser, Human oocyte vitrification: the permeability of metaphase II oocytes to water and ethylene glycol and the appliance toward vitrification, *Fertil. Steril.* 89 (2008) 1812–1825.
- [27] S.J. Paynter, B.J. Fuller, R.W. Shaw, Temperature dependence of mature mouse oocyte membrane permeabilities in the presence of cryoprotectant, *Cryobiology* 34 (1997) 122–130.
- [28] S.J. Paynter, L. O'Neil, B.J. Fuller, R.W. Shaw, Membrane permeability of human oocytes in the presence of the cryoprotectant propane-1,2-diol, *Fertil. Steril.* 75 (2001) 532–538.
- [29] L.E. McGann, A.R. Turner, J.M. Turc, Microcomputer interface for rapid measurements of average volume using an electronic particle counter, *Med. Biol. Eng. Comput.* 20 (1982) 117–120.
- [30] C.M. Kashuba, J.D. Benson, J.K. Critser, Rationally optimized cryopreservation of multiple mouse embryonic stem cell lines: I-comparative fundamental cryobiology of multiple mouse embryonic stem cell lines and the implications for embryonic stem cell cryopreservation protocols, *Cryobiology* 68 (2) (2014) 166–175.
- [31] C.M. Kashuba Benson, J.D. Benson, J.K. Critser, An improved cryopreservation method for a mouse embryonic stem cell line, *Cryobiology* 56 (2008) 120–130.
- [32] R.E. Lusianti, J.D. Benson, J.P. Acker, A.Z. Higgins, Rapid removal of glycerol from frozen-thawed red blood cells, *Biotechnol. Prog.* 69 (2013) 609–620.
- [33] J.A. Gilmore, J. Liu, E.J. Woods, A.T. Peter, J.K. Critser, Cryoprotective agent and temperature effects on human sperm membrane permeabilities: convergence of theoretical and empirical approaches for optimal cryopreservation methods, *Hum. Reprod.* 15 (2000) 335–343.
- [34] J.D. Benson, E.J. Woods, E.M. Walters, J.K. Critser, The cryobiology of spermatozoa, *Theriogenology* 78 (2012) 1682–1699.
- [35] A. Chaveiro, J. Liu, B. Engel, J.K. Critser, H. Woelders, Significant variability among bulls in the sperm membrane permeability for water and glycerol: possible implications for semen freezing protocols for individual males, *Cryobiology* 53 (2006) 349–359.
- [36] Y.P. Zee, W.V. Holt, V. Nicolson, M. Pyne, S.D. Johnston, Individual variability in post-thaw sperm survival in a captive koala population, *Cryobiology* 59 (2009) 69–74.
- [37] Y. Wu, J.D. Benson, M. Almasri, "MEMS coulter counters for studying time sensitive cells," *biomed, Microdevices* 14 (2012) 739–750.
- [38] M. Brown, C. Wittwer, Flow cytometry: principles and clinical applications in hematology, *Clin. Chem.* 46 (2000) 1221–1229.
- [39] R.D. Eastham, Rapid whole-blood platelet counting using an electronic particle counter, *J. Clin. Pathol.* 16 (1963) 168–169.
- [40] D. Spencer, V. Hollis, H. Morgan, Microfluidic impedance cytometry of tumour cells in blood, *Biomicrofluidics* 8 (2014), 064124-064131-064124-064211.
- [41] Z. Ma, P. Zhang, Y. Cheng, S. Xie, S. Zhang, X. Ye, Homogeneous agglutination assay based on micro-chip sheathless flow cytometry, *Biomicrofluidics* 9 (2015), 066501-1-066501-066511.
- [42] E. Salimi, K. Braasch, M. Butler, D.J. Thomson, G.E. Bridges, Dielectric model for Chinese hamster ovary cells obtained by dielectrophoresis cytometry, *Biomicrofluidics* 10 (2016), 014111-1-014111-014115.
- [43] X. Mao, A.A. Nawaz, S.S. Lin, M.I. Lapsley, Y. Zhao, J.P. McCoy, W.S. El-Deiry, T.J. Huang, "An integrated, multiparametric flow cytometry chip using "microfluidic drifting" based three-dimensional hydrodynamic focusing, *Biomicrofluidics* 6 (2012), 024113-024121-024113-024119.
- [44] B. Patra, Y. Chen, C. Peng, S. Lin, C. Lee, Y. Tung, A microfluidic device for uniform-sized cell spheroids formation, culture, harvesting and flow cytometry analysis, *Biomicrofluidics* 7 (2013), 054114-054121-054114-054211.
- [45] M. Nikolic-Jaric, T. Cabel, E. Salimi, A. Bhide, K. Braasch, M. Butler, G.E. Bridges, D.J. Thomson, Differential electronic detector to monitor apoptosis using

- dielectrophoresis-induced translation of flowing cells (dielectrophoresis cytometry), *Biomicrofluidics* 7 (2013), 024101-1-024101-024114.
- [46] A. Alshalani, A. Howell, J.P. Acker, Impact of blood manufacturing and donor characteristics on membrane water permeability and in vitro quality parameters during hypothermic storage of red blood cells, *Cryobiology* 80 (2018) 30–37.
- [47] A. Alshalani, J.P. Acker, Red blood cell membrane water permeability increases with length of ex vivo storage, *Cryobiology* 76 (2017) 51–58.
- [48] H. Zhang, C.H. Chon, X. Pan, D. Li, Methods for counting particles in microfluidic applications, *Microfluid. Nanofluidics* 7 (2009) 739–749.
- [49] D. Anselmetti, Nanopores: tiny holes with great promise, *Nat. Nanotechnol.* 7 (2012) 81–82.
- [50] O.A. Saleh, L.L. Sohn, An artificial nanopore for molecular sensing, *Nano Lett.* 3 (2003) 37–38.
- [51] D.A. Ateya, J.S. Erickson, P.B. Jr Howell, L.R. Hilliard, J.P. Golden, F.S. Ligler, The good, the bad, and the tiny: a review of microflow cytometry, *Anal. Bioanal. Chem.* 391 (2008) 1485–1498.
- [52] H. Yin, D. Marshall, Microfluidics for single cell analysis, *Curr. Opin. Biotechnol.* 23 (1) (2012) 110–119.
- [53] Y. Wu, J.D. Benson, M. Almasri, "MEMS coulter counters for studying time sensitive cells," *biomed. Microdevices* 14 (2012) 739–750.
- [54] M. Korampally, J.D. Benson, Y. Wu, J.K. Critser, M. Almasri, A mems-based coulter counter for cell sizing, in: *Proc. SPIE 6886, Microfluidics, BioMEMS, and Medical Microsystems VI*, 2008, 68860A.
- [55] Y. Wu, J.D. Benson, M. Almasri, Micromachined coulter counter for dynamic impedance study of time sensitive cells, *Biomed. Microdevices* 14 (2012) 739–750.
- [56] Y. Wu, J.D. Benson, J.K. Critser, M. Almasri, Mems-based coulter counter for cell counting and sizing using multiple electrodes, *J. Micromech. Microeng.* 20 (2010), 085035, 085047.
- [57] Y. Wu, J.D. Benson, J.K. Critser, M. Almasri, Microelectromechanical systems coulter counter for cell monitoring and counting, *Rev. Sci. Instrum.* 81 (2010), 076103, 076113.
- [58] J. Schaber, E. Klipp, Short-term volume and turgor regulation in yeast, *Essays Biochem.* 45 (2008) 147–160.
- [59] R. Pethig, Dielectrophoresis: status of the theory, technology, and applications, *Biomicrofluidics* 4 (2010) 22811, 1–022811-35.
- [60] W.S. Rasband, ImageJ, U. S. National Institutes of Health, Bethesda, Maryland, USA, 1997-2015, <http://imagej.nih.gov/ij/>.
- [61] F. Dumont, P-A. Marechal, P. Gervais, "Cell size and water permeability as determining factors for cell viability after freezing at different cooling rates," *Appl. Environ. Microbiol.*, vol. 70(1), pp. 268–2722004.
- [62] A.L. Richards, M.D. Dickey, A.S. Kennedy, G.D. Buckner, Design and demonstration of a novel micro-Coulter counter utilizing liquid metal electrodes, *J. Micromech. Microeng.* 22 115012 (2012), <https://doi.org/10.1088/0960-1317/22/11/115012>.
- [63] R. DeBlois, C.P. Bean, Electrokinetic measurements with submicron particles and pores by the resistive pulse technique, *J. Colloid Interface Sci.* 61 (2) (1977).
- [64] A.Z. Higgins, J.O.M. Karlsson, Curve fitting approach for measurement of cellular osmotic properties by the electrical sensing zone method. I. Osmotically inactive volume, *Cryobiology* 57 (3) (2008) 223–233.
- [65] A.K. Bryan, A. Goranov, A. Amon, S.R. Manalis, Measurement of mass, density, and volume during the cell cycle of yeast, *Proc. Natl. Acad. Sci. Unit. States Am.* 107 (3) (2010) 999–1004.